Chemical Engineering Journal 150 (2009) 502–508

Contents lists available at ScienceDirect

Chemical Engineering Journal

journal homepage: www.elsevier.com/locate/cej

Heat transfer model of a solar receiver-reactor for the thermal dissociation of ZnO—Experimental validation at 10 kW and scale-up to 1 MW

L.O. Schunk[a], W. Lipiński[b], A. Steinfeld[a,c,*]

[a] Solar Technology Laboratory, Paul Scherrer Institute, 5232 Villigen PSI, Switzerland
[b] Department of Mechanical Engineering, University of Minnesota, Minneapolis, MN 55455, USA
[c] Department of Mechanical and Process Engineering, ETH Zurich, 8092 Zurich, Switzerland

ARTICLE INFO

Article history:
Received 10 November 2008
Received in revised form 3 March 2009
Accepted 4 March 2009

Keywords:
Zinc
Oxide
Dissociation
Ablation
Water splitting
Thermochemical
Cycle
Hydrogen
Solar
Energy
Reactor
Heat transfer
Radiation

ABSTRACT

A transient heat transfer model is developed for analyzing the thermal performance of a thermochemical reactor for the solar-driven dissociation of ZnO in the 1600–2136 K range. The reactor consists of a rotating cavity-receiver lined with ZnO particles that are directly exposed to concentrated solar radiation. The model couples radiation, convection, and conduction heat transfer to the reaction kinetics for a shrinking domain and simulates a transient ablation regime with semi-batch feed cycles of ZnO particles. Validation is accomplished in terms of the numerically calculated and experimentally measured temperature profiles and reaction extents for a 10 kW reactor prototype tested in a high-flux solar simulator and subjected to peak solar concentration ratios exceeding 5000 suns. Scaling-up the reactor technology to 1 MW solar thermal power input has the potential of reaching a solar-to-chemical energy conversion efficiency of 56%.

1. Introduction

Solar thermochemical H_2O-splitting processes utilize concentrated solar radiation as the energy source of high-temperature process heat [1]. Several cycles based on metal oxides redox reactions are being considered [2–5]. Of special interest is the one based on the ZnO/Zn redox pair, comprising: (1) the solar endothermal dissociation of ZnO(s) at above 2000 K and (2) the non-solar exothermal hydrolysis of Zn into H_2 and ZnO(s), and represented by

1st step (solar ZnO-dissociation):

$$ZnO \rightarrow Zn + 0.5O_2 \quad \Delta H^{\circ}_{298\,K} = 350\,kJ\,mol^{-1} \tag{1}$$

2nd step (non-solar Zn-hydrolysis):

$$Zn + H_2O \rightarrow ZnO + H_2 \quad \Delta H^{\circ}_{298\,K} = -64.7\,kJ\,mol^{-1} \tag{2}$$

This cycle has been identified as a promising path for solar hydrogen production from water because of its potential for reaching high energy conversion efficiencies and, consequently, economic competitiveness [6,7]. The 2nd step of the cycle has been experimentally demonstrated using a separate aerosol-flow reactor for in situ formation and hydrolysis of Zn nanoparticles [8]. This paper deals with the solar reactor technology for performing the 1st step of the cycle.

Solar chemical reactors for effecting high-temperature gas–solid transformations usually employ cavities containing directly irradiated reacting particles [9,10]. The direct irradiation of the chemical reactants provides efficient energy transfer to the reaction site, circumventing the limitations imposed by indirect heat transfer through reactor walls. Recently, a 10 kW solar reactor prototype based on this concept has been designed and tested [11]. This reactor features a rotating cavity-receiver lined with ZnO particles that are directly exposed to concentrated solar radiation and serve simultaneously the functions of radiant absorbers and chemical reactants. A heat transfer model was initially formulated for a simplified reactor geometry, neglecting the semi-batch feeding mode of operation and the shrinkage of the ZnO layer [12]. These simplifications limited its applicability for the optimization and scale-up of the reactor technology, since matching the rate of heat trans-

* Corresponding author at: Department of Mechanical and Process Engineering, ETH Zurich, 8092 Zurich, Switzerland. Tel.: +41 44 6327929; fax: +41 44 6321065.
E-mail address: aldo.steinfeld@eth.ch (A. Steinfeld).

1385-8947/$ – see front matter © 2009 Elsevier B.V. All rights reserved.
doi:10.1016/j.cej.2009.03.012

Nomenclature

A	surface area, m^2
c_p	specific heat capacity, $J\,kg^{-1}\,K^{-1}$
d	diameter, m
E_a	activation energy, $kJ\,mol^{-1}$
F	configuration factor
h	convective heat transfer coefficient, $W\,m^{-2}\,K^{-1}$
H_r	reaction enthalpy, $J\,kg^{-1}$
k	thermal conductivity, $W\,m^{-1}\,K^{-1}$
k_0	frequency factor, $kg\,m^{-3}\,s^{-1}$
L	cavity length, m
m	mass, kg
n	index of refraction
$\hat{n}$	unit normal vector
N	number of elements
p	porosity
P	radiation power input, W
q''	heat flux, $W\,m^{-2}$
q'''	volumetric heat sink, $W\,m^{-3}$
r	radius
r	reaction rate, $kg\,s^{-1}$
r'''	reaction rate, $kg\,m^{-3}\,s^{-1}$
R	universal gas constant, $J\,mol^{-1}\,K^{-1}$
t	time, s
T	temperature, K
V	volume, m^3

Greek symbols

α	rim angle of the incoming solar radiation
β	extinction coefficient, m^{-1}
ε	emissivity
ρ	density, $kg\,m^{-3}$
η	solar-to-chemical energy conversion efficiency
ν	kinematic viscosity, $m^2\,s^{-1}$
σ	Stefan–Boltzmann constant, $W\,m^{-2}\,K^{-4}$
ω	angular frequency, s^{-1}

Subscripts

eff	effective
out	at the outer surfaces of the reactor
inn	at the inner surfaces of the cavity
0	initial

Dimensionless groups

Ra	Rayleigh number
Nu	Nusselt number
Pr	Prandtl number

fer to the rate of the chemical reaction is needed for maximizing its energy conversion efficiency. In a follow-up study, the effect of sintering and shrinkage on the rate of heat transfer was examined for a packed-bed of ZnO particles subjected to solar flux concentration ratios in the range 1225–2133 suns and surface temperatures in the range 1834–2109 K [13]. Operating conditions were typical of an ablation regime controlled by the rate of radiative heat transfer to the first layers of ZnO undergoing endothermic dissociation. This previous analysis served to determine the effective thermal transport properties of the ZnO packed-bed, namely the extinction coefficient, the surface absorptivity, and the effective thermal conductivity.

In this paper, the reactor model is expanded to consider the exact 3D geometry of the cavity, the actual semi-batch feeding mode of ZnO particles, and the fact that the packed-bed layer of ZnO particles lining the cavity shrinks as the reaction progresses. Further, a more accurate kinetic rate law derived from experimental measurements in a solar-driven thermogravimeter for directly irradiated ZnO samples is incorporated into the model [14]. Validation is accomplished by comparing the numerically calculated and experimentally measured temperatures and reactions extents for a 10 kW reactor prototype tested in a high-flux solar simulator. The model is then applied to optimize the reactor engineering design and to analyze the thermal performance of 100 kW and 1 MW scaled-up reactors.

2. Solar reactor configuration

The solar reactor configuration is shown schematically in Fig. 1a; its cross sectional view is shown in Fig. 1b. It has been previously described in detail [11]; only the main features are summarized here. The principal component is a rotating cylindrical cavity (#1) composed of sintered ZnO tiles glued on top of porous 80%Al_2O_3–20%SiO_2 insulation (#2) and wrapped with 95%Al_2O_3–5%Y_2O_3 ceramic matrix composite (CMC; #3), to provide mechanical, thermal, and chemical stability and a diffusion barrier for product gases. The volume between the CMC and the Al-mantle (#5) is packed with Al_2O_3 insulating fibers (#4). The cavity contains a circular opening – the *aperture* (#6) – to let in concentrated solar radiation through a quartz window (#7) mounted on a water-cooled Al-ring and integrated to the front face of the cavity via a conical frustum (#9). The reactor has a dynamic feeder (#8) that extends and retracts within the cavity, allowing for batches of an evenly distributed layer of ZnO particles of desired thickness over the entire cavity surface. The rotational movement along the horizontal axis generates a centripetal acceleration that forces the ZnO particles to cover the cavity wall, thereby, creating an efficient use of the cavity space for radiation heat transfer to the reaction site. 3D computational fluid dynamics (CFD) was employed to determine the optimal flow configuration for an aerodynamic protection of the quartz window against condensable Zn(g) [11]. CFD was also employed for the design of the quenching apparatus incorporated at the exit of the solar reactor for the purpose of avoiding product recombination [28]. A 10 kW reactor prototype was fabricated: a 160 mm-dia. 230 mm-length cylindrical cavity containing a 60 mm-dia. aperture with a 3 mm-thick quartz window.

Experimentation was carried out at the high-flux solar simulator (HFSS) of the Paul Scherrer Institute [15], comprised an array of 10 high-pressure Xenon arcs, each close-coupled with truncated ellipsoidal specular reflectors of common focus. This research facility provides an external source of intense thermal radiation (radiative power >50 kW, solar concentration ratio >10,000 suns[1]) that closely approximates the heat transfer characteristics of highly concentrating solar systems such as towers, dishes, and furnaces. Solar power fluxes q''_{solar} incident on the focal plane were measured optically with a calibrated CCD camera on a water-cooled Al_2O_3-coated Lambertian target. Integration of q''_{solar} over the reactor's aperture yielded the total power entering the cavity, P_{solar}. The transient temperature profiles were measured with type-K and type-B thermocouples placed at the backside of the ZnO cavity tiles and in the reactor insulation, as indicated in Fig. 1b. Gas mass flow rates were measured with electronic flow meters (Bronkhorst). Argon was injected through radial and tangential nozzles located around the frustum, creating an aerodynamic curtain that protected the window from Zn(g) condensation. The mass flow rate of Ar for keeping the window clean and carrying the gaseous products was in the

[1] Solar concentration ratio is defined as the mean solar radiative flux over the aperture normalized to 1 kW/m², and is usually given in units of "suns".

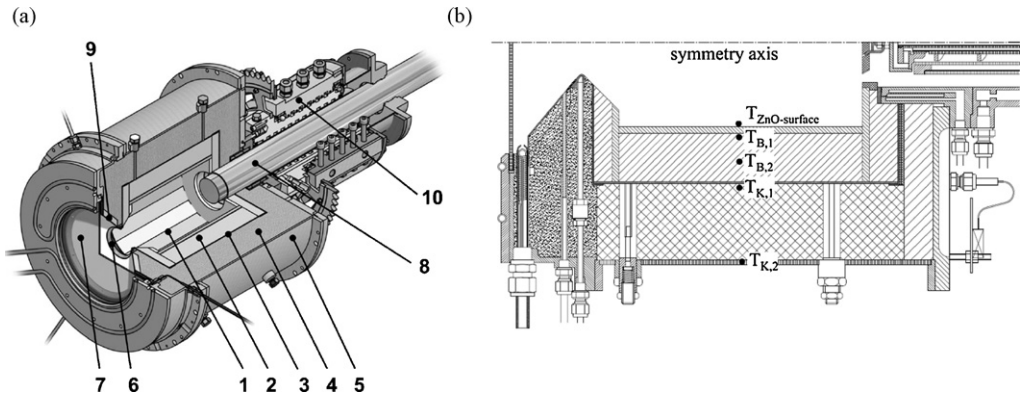

Fig. 1. (a) Schematic of the solar chemical reactor configuration: 1 = rotating cavity lined with sintered ZnO tiles, 2 = 80%Al_2O_3–20%SiO_2 insulation, 3 = 95%Al_2O_3–5%Y_2O_3 CMC, 4 = alumina fibers, 5 = Al reactor mantle, 6 = aperture, 7 = quartz window, 8 = dynamic feeder, 9 = conical frustum, 10 = rotary joint. (b) Cross section of the solar chemical reactor. Indicated are the locations of temperature measurements with type-B and type-K thermocouples.

range 0.32–0.49 g s^{-1} [11]. The rotational speed of the cavity was in the range 30–120 rpm.

3. Heat transfer analysis

The unsteady-state energy conservation equation is given by

$$\rho c_p \frac{\partial T}{\partial t} = \nabla(k_{\text{eff}} \nabla T) + q'''_{\text{chemistry}} \tag{3}$$

$q'''_{\text{chemistry}}$ is the volumetric heat sink rate due to the endothermic dissociation of ZnO,

$$q'''_{\text{chemistry}} = -r''' \Delta H_r(T) \tag{4}$$

where the enthalpy change of the reaction, Eq. (1), is in J kg^{-1} [16]:

$$\Delta H_r(T) = 5.96 \times 10^6 - 161.32T - 2.66 \times 10^{-2} T^2 \tag{5}$$

and the reaction rate is modeled by applying a zero-order Arrhenius-type rate law [14]

$$r''' = k_0 \exp\left(-\frac{E_a}{RT}\right) \tag{6}$$

with E_a = 361 kJ mol^{-1} experimentally determined in a solar-driven thermogravimeter for directly irradiated ZnO samples [14]. The frequency factor, $k_0 = 2.81 \times 10^9$ kg m^{-3} s^{-1}, has been adjusted to fit the rates obtained in the solar reactor, as they were affected by convective mass transport at the ZnO surface. The boundary and initial conditions are:

at the inner surfaces of the cavity,

$$k_{\text{eff}} \nabla T \cdot \hat{n} = h_{\text{inn}}(T - T_{\text{gas}}) + q''_{\text{radiative}} \tag{7}$$

at the outer walls of the reactor,

$$k_{\text{eff}} \nabla T \cdot \hat{n} = h_{\text{out}}(T_{\text{ambient}} - T) + \varepsilon\sigma(T^4_{\text{ambient}} - T^4) \tag{8}$$

$$T(x, r, t = 0) = T_0 \tag{9}$$

The effective thermal conductivity is given by the sum of the conductive and radiative contributions, $k_{\text{eff}} = k_{\text{conductive}} + k_{\text{radiative}}$ [13]. For the optically thick packed-bed of ZnO, the Rosseland diffusion approximation [17] is applied:

$$k_{\text{radiative}} = \frac{16n^2}{3\beta}\sigma T^3 \tag{10}$$

with $\beta = 1900\ \text{m}^{-1}$ [13]. For the porous packed-bed [18]:

$$k_{\text{conductive}} = k_{\text{gas}} \left[1 - \sqrt{1-p} + \sqrt{1-p}\frac{2}{A} \left(\frac{(1 - k_{\text{gas}}/k)B}{A^2} \ln\frac{k}{Bk_{\text{gas}}} - \frac{B+1}{2} - \frac{B-1}{A}\right)\right] \tag{11}$$

with $A = 1 - (k_{\text{gas}}/k)B$, $B = 1.25(1-p/p)^{10/9}$. The porosity p was assumed zero for the 10 kW reactor (based on experimental observation) and varied in the range 0–0.5 for the scaled-up design. The convective heat transfer coefficients h_{inn}, h_{out}, and $h_{\text{out,window}}$ at the inner surfaces of the cavity, external walls of the Al-mantle, and window, respectively, were determined by CFD simulations [19] and using the correlations [20–22]:

$$\text{Nu}_{\text{out}} = 0.318\left(\frac{\omega d^2}{2\nu}\right)^{0.571} \tag{12}$$

$$\text{Nu}_{\text{out,window}} = \left(0.825 + \frac{0.387\ \text{Ra}^{1/6}}{\left[1 + (0.492/Pr)^{9/16}\right]^{8/27}}\right)^2 + 1.855\left(\frac{\omega d^2}{2\nu}\right)^{0.4} \tag{13}$$

varied in the range 100–780 W m^{-2} K^{-1}. h_{out} = 6.17 W m^{-2} K^{-1} and $h_{\text{out,window}}$ = 23 W m^{-2} K^{-1} for an angular velocity ω = 11.1 s^{-1} and characteristic lengths d = 0.4 m (outer diameter), and d = 0.24 m (window diameter), respectively. Radiative exchange in the cavity is modeled by assuming directional incident solar radiation and diffuse emission by the cavity walls. The net heat source to element A_i arising from the solar radiation, is modeled $q''_{\text{solar},i}$ by applying Monte Carlo ray tracing method (MC), which accounts for the complete exchange process of the solar radiation between all cavity elements [15,23]. The radiosity method (enclosure theory) [17] is applied to obtain the net radiative flux arising from q''_{walls} radiation emitted by the cavity walls. The corresponding system of equations is given by

$$q''_{\text{radiative},i} = q''_{\text{walls},i} - q''_{\text{solar},i} \tag{14}$$

$$\sum_{i=1}^{N}\left(\frac{\delta_{ki}}{\varepsilon_i} - F_{k-i}\frac{1-\varepsilon_i}{\varepsilon_i}\right) q''_{\text{walls},i} = \sum_{i=1}^{N}(\delta_{ki} - F_{k-i})\sigma T_i^4 \tag{15}$$

where $\delta_{ki} = 1$ when $k = i$ and $\delta_{ki} = 0$ when $k \neq i$. The configuration factors F_{k-i} are calculated by MC with 10^8 rays emitted from each inner surface. Eq. (15) is solved iteratively for $N = 92$ by matrix inversion using the Gauss–Seidel numerical algorithm. The water-cooled components (Al-front shield, aperture, and quench section) are modeled as solids at 297 K. The frustum and cavity surfaces are assumed grey-diffuse surfaces. The window is treated as perfectly transparent for incident solar radiation and as opaque grey-diffuse for IR radiation emitted by the inner surfaces of the cavity. The finite volume method and the explicit Euler time integration scheme are applied to solve the integrated form of Eq. (3) over a finite time step Δt and over shrinking annular elements ΔV. As the reaction progresses at a rate r_i''' and the ZnO layers shrink, the thickness Δr of a finite ZnO annular element with outer radius r_2 varies according to

$$\Delta r = r_2 - \sqrt{r_2^2 - \frac{1}{L\pi\rho}\sum_{i=1}^{N_{\text{cavity}}}(\Delta m_i - r'''_i\,\Delta V_i\,\Delta t)} \tag{16}$$

Finally, the cyclic batch-feeding of ZnO particles is modeled by adding finite volumes to the numerical domain. The baseline parameters used in the numerical simulation are listed in Table 1.

4. Model validation

A set of four experimental runs with 3, 5, 7, and 9 consecutive feed-cycles was used to validate the reactor model. A typical run consisted of three phases: (1) heating, (2) feeding and dissociation, and (3) cooling. Firstly, the reactor's cavity was heated to 1600 K within approximately 1 h by igniting stepwise the arcs of the HFSS and delivering from 1.6 kW to 5.7 kW through the reactor's aperture. During this heating phase, the cavity temperature was not allowed to exceed 1630 K in order to prevent the unprotected irradiated ZnO tiles from dissociating. In the second phase, the screw-feeder was extended into the cavity and ZnO particles were spread uniformly over the rotating cavity walls. To avoid overheating of the feeder's cap, the power input P_{solar} from the HFSS was interrupted briefly (~50 s) during the duration of the feeding. Afterwards, the radiative power was re-established and further increased up to 10 kW while the cavity temperature was maintained in the range 1840–1980 K. The batch feed-cycles were repeated. In the third phase, the HFSS was shut down and the reactor underwent cooling while keeping the Ar flow.

Fig. 2a, b, c, and d show the experimentally measured (solid curves) and numerically calculated (dashed curves) temperatures at locations $T_{B,1}$, $T_{B,2}$, $T_{K,1}$, and $T_{K,2}$ for the four runs with 3, 5, 7, and 9 consecutive feed-cycles, respectively. Also indicated are the measured power input and the calculated dissociation rate of ZnO. The arrows on top of the figure point out to the times when the batch feeding of ZnO took place. The temperature agreement is reasonably good at all location for all 4 runs. As expected, temperatures dropped during ZnO-feeding due to the interruption of P_{solar} and the addition of fresh ZnO particles. Discrepancies are attributed to slow and partial mixing of hot residual and cold fresh particles (not modeled). Note that pyrometry could not be applied to measure the ZnO surface temperature $T_{\text{ZnO-surface}}$ or the window temperature T_w because of the intense reflected radiation over a wide spectrum. The calculated value of $T_{\text{ZnO-surface}}$, typically 30 K above $T_{B,1}$, compared well with that measured in a solar furnace where a solar-blind pyrometer could be used [12]. The maximum calculated value of T_w was 1299 K at $T_{\text{ZnO-surface}} = 1974$ K (5 feed-cycle run) and agreed with the measured value of $T_w \sim 1300$ K at $T_{\text{ZnO-surface}} = 1970$ K [24]. The reaction rate increased as $T_{\text{ZnO-surface}}$ exceeded 1700 K, dropped to zero during ZnO-feeding, and climbed up to 40 mg s^{-1} as P_{solar} was resumed and the temperature levels re-established. The maximum power input was 9.9 kW, which corresponds to a peak solar

Table 1
Baseline parameters used in the numerical simulation.

	Value	Range (K)	Unit
$c_{p,Al2O3}$ [a]	$-4.33\times10^{-9}T^4 + 1.24\times10^{-5}T^3 - 1.39\times10^{-2}T^2 + 7.53T - 528.0$ $-3.85\times10^{-11}T^4 + 2.69\times10^{-7}T^3 - 7.12\times10^{-4}T^2 + 9.56\times10^{-1}T - 745.65$	$293 \le T \le 810$ $810 < T \le 2100$	J kg^{-1} K^{-1}
$c_{p,ZnO}$ [a]	$-3.03\times10^{-9}T^4 + 7.34\times10^{-6}T^3 - 6.80\times10^{-3}T^2 + 3.01T + 41.6$ $-1.06\times10^{-5}T^2 + 1.27\times10^{-1}T + 3.0T + 522.6$	$293 \le T \le 693$ $693 < T \le 2000$	J kg^{-1} K^{-1}
$c_{p,mantle}$ [a]	927 (alumina); 501 (steel)	$T = 293$	J kg^{-1} K^{-1}
$c_{p,SiO2}$ [a]	$-1.80\times10^{-3}T^2 + 2.59T + 122.73$ $-1.03\times10^{-10}T^4 + 6.20\times10^{-7}T^3 - 1.40\times10^{-3}T^2 + 1.50T + 525.83$	$293 \le T \le 543$ $543 < T \le 2000$	J kg^{-1} K^{-1}
$c_{p,window}$ [a]	$-7.06\times10^{-12}T^5 + 1.88\times10^{-8}T^4 - 1.70\times10^{-5}T^3 + 4.46\times10^{-3}T^2 + 1.93T + 61.5$ $3.14\times10^{-8}T^3 - 1.11\times10^{-4}T^4 + 3.71\times10^{-1}T + 890.24$	$115 \le T \le 925$ $925 < T \le 2000$	J kg^{-1} K^{-1}
k_{Al2O3} [a]	$1.78\times10^{-11}T^4 - 9.79\times10^{-8}T^3 + 2.02\times10^{-4}T^2 - 1.90\times10^{-1}T + 75.77$	$293 < T < 2073$	W m^{-1} K^{-1}
$k_{insulation}$ [b]	$1.07\times10^{-7}T^2 - 8.35\times10^{-5}T + 0.17$	$293 < T < 2073$	W m^{-1} K^{-1}
k_{mantle}	220 (alumina); 42 (steel)	$T = 293$	W m^{-1} K^{-1}
k_{window} [a]	$1.31\times10^{-14}T^5 - 5.01\times10^{-11}T^4 + 7.55\times10^{-8}T^3 - 5.29\times10^{-5}T^2 + 1.82\times10^{-2}T - 9.85\times10^{-1}$	$293 < T < 1400$	W m^{-1} K^{-1}
k_{ZnO} [c]	$59.15\exp(-2\times10^{-3}T)$	$293 < T < 2100$	W m^{-1} K^{-1}
T_0	293	$T = 293$	K
ε	0.2 (aperture); 0.69 (ZnO); 0.8 (Al_2O_3); 0.9 (window); 0.2 (mantle)		
ρ_{Al2O3}	3924	$T = 293$	kg m^{-3}
$\rho_{insulation}$ [b]	400	$T = 293$	kg m^{-3}
ρ_{mantle}	2700 (alumina Al99.5), 7860 (steel St 35)	$T = 293$	kg m^{-3}
ρ_{window} [a]	2220	$T = 293$	kg m^{-3}
ρ_{ZnO}	5550	$T = 293$	kg m^{-3}

[a] Ref. [30].
[b] Ref. [31].
[c] Ref. [32].

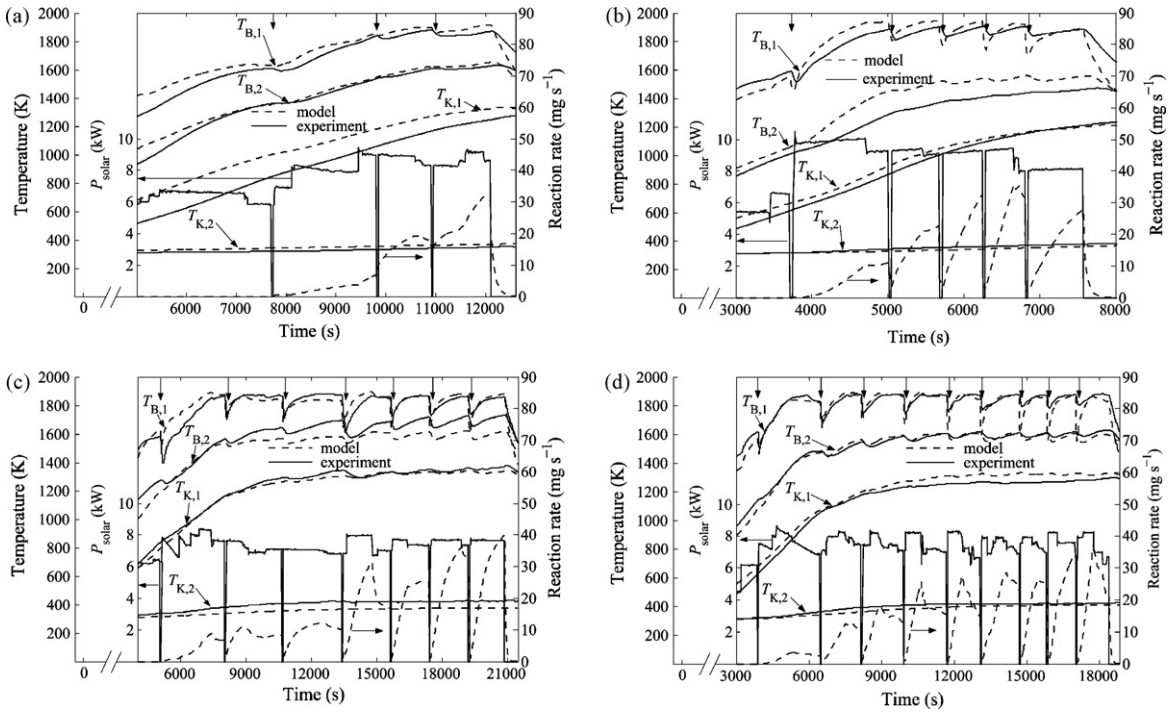

Fig. 2. Experimentally measured (solid curves) and numerically calculated (dashed curves) temperatures halfway along the reactor cavity at locations $T_{B,1}$, $T_{B,2}$, $T_{K,1}$, $T_{K,2}$ (see locations in Fig. 1b), measured radiation power input P_{solar}, and numerically calculated ZnO-dissociation rate as a function of time for a set of four experimental runs with (a) 3, (b) 5, (c) 7, and (d) 9 feed-cycles. The top arrows point out to the times when the batch feeding of ZnO took place.

concentration ratio of 5600 suns and a mean of 3490 suns over the aperture.

Table 2 lists the experimentally measured mass of ZnO dissociated during the complete run and the numerically calculated mass that is obtained by integrating the dissociation rate of ZnO for the 4 runs shown in Fig. 2a–d. Reasonable good agreement in the mass balance is found for all 4 runs. The observed differences between the measured and calculated ZnO mass for the 7 feed-cycle run is attributed to partial clogging at the reactor outlet. The model is able to corroborate the experimental observation that the ZnO dissociation reaction occurred in the topmost layers at the highest temperatures, which is typical of an ablation regime as radiative heat transfer to the endothermic reaction proceeded at a faster rate than heat conduction across the packed-bed.

Fig. 3 shows the instantaneous energy balance as a function of time for the run with 9 feed-cycles, corresponding to Fig. 2d. Indicated is the heat consumed by the endothermic reaction (including the sensible heat of dissociated ZnO), the sensible heat of reactor components, and the heat losses by conduction, convection, and re-radiation. Heating the reactor materials consumes 13.1% of P_{solar}. Conductive losses to the water-cooled front shield, aperture, and quench amount to 46.7% of P_{solar}. Radiative losses through the aperture and annular exit amount to 18.7 and 11.5% of P_{solar}, respectively. Convective losses from the reactor mantle amounts to 8.9% of P_{solar}.

Table 2
Measured amount of ZnO dissociated during experimental runs with 3, 5, 7, and 9 feed-cycles and the corresponding amount obtained by integrating the numerically calculated ZnO dissociation rate.

# feed-cycles	ZnO dissociated (g)	
	Measured	Calculated
3	68.5 ± 5.2	63.9
5	59.5 ± 6.8	54.0
7	148.4 ± 28.8	223.3
9	224.2 ± 49.5	197.1

The solar-to-chemical energy conversion efficiency is defined as

$$\eta = \frac{r\left(H_r(T) + \int_{T_0}^{T} c_{p,\mathrm{ZnO}}\, dT\right)}{P_{solar}} \tag{17}$$

η was only 1.1% when integrated over the complete run of Fig. 3. The highest value obtained experimentally was $\eta = 3.1\%$ for $P_{solar} = 11.1$ kW, as higher operating temperatures were reached and, consequently, higher reaction rates were induced. An increase of only 20% in P_{solar} translated to an increase of 190% in the reaction rate and to $\eta = 2.9\%$. Nevertheless, substantial conduction heat losses to the water-cooled components remained the major source

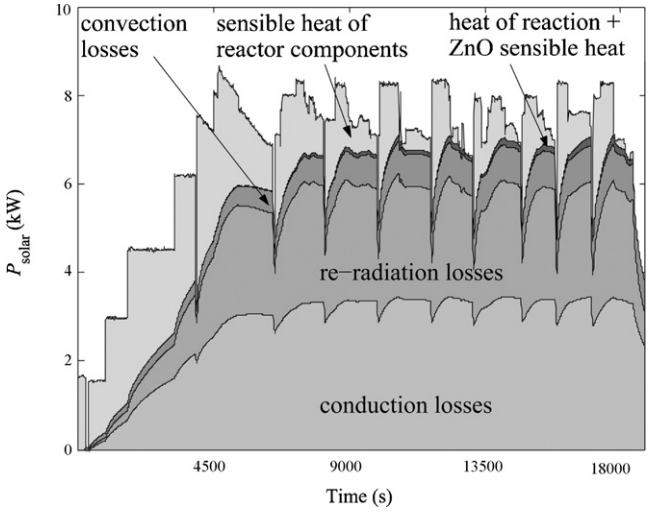

Fig. 3. Instantaneous energy balance of the experimental run with 9 feed-cycles. Indicated are the heat consumed by the endothermic reaction (including the sensible heat of dissociated ZnO), the sensible heat of reactor components, and the heat losses by conduction, convection, and re-radiation.

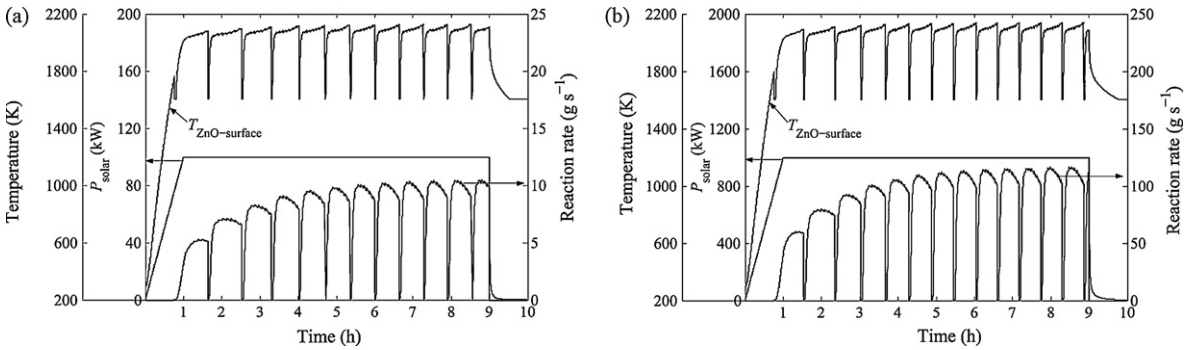

Fig. 4. Solar power input, ZnO surface temperature halfway along the reactor cavity, and ZnO-dissociation rate as a function of time for a typical day of operation at $P_{solar,nominal}$ = 100 kW (a) and 1000 kW (b).

of inefficiency (46.7% of P_{solar}) for the 10 kW prototype reactor. Optimizing the prototype reactor geometry by downsizing the size of the cavity exit from d = 80 mm to d = 30 mm and by removing the exit's water-cooling yielded η = 16.9%.

5. Reactor scale-up

The heat transfer model is employed to predict the thermal performance of a scaled-up reactor during a typical day operation for a nominal power input $P_{solar,nominal}$ = 100 and 1000 kW. Dimensions are listed in Table 3. The aperture size is set for an average solar concentration ratio of 3500 suns. q''_{solar} is assumed to be uniformly distributed over the inner surfaces of the cavity. Feeding a new batch of ZnO particles takes place once the ZnO-layer thickness has decreased by 60%. P_{solar} is increased linearly from zero to $P_{solar,nominal}$ within the first hour, held constant for 8 h, and then set to zero for shut down. Variation of p in the range 0–0.5 and of β in the range 1900–7850 m^{-1} [13,25] account for the uncertainties of the values assigned to these two properties of the ZnO-layer. Baseline values used are p = 0.5 and β = 7850 m^{-1}. The extinction coefficient of the porous ZnO is $\beta_{porous} = (1-p)\beta$ [26].

The solar power input, reaction rate, and ZnO surface temperature are shown in Fig. 4a and b as a function of time for a typical day operation of the 100 and 1 000 kW reactors, respectively. Heating from ambient to $T_{ZnO\text{-}surface}$ = 2000 K takes about 1 h for both reactors. Twelve and fourteen feed-cycles of 20 and 200 kg ZnO each are performed for the 100 and 1000 kW reactors, respectively. For the 100 kW reactor, the reaction rate increases from 3.4 g s^{-1} at t = 1 h to 10.5 g s^{-1} by $T_{ZnO\text{-}surface}$ = 2126 K towards the end of the day. For the 1000 kW reactor, the reaction rate increases from 43.0 g s^{-1} at t = 1 h to 116.9 g s^{-1} by $T_{ZnO\text{-}surface}$ = 2136 K towards the end of the day. As already observed in the 10 kW prototype, the reaction rate drops to zero during ZnO feeding as a result of the drop in $T_{ZnO\text{-}surface}$. Temperature distributions after 7 h are shown in Fig. 5 for the 100 kW reactor. These are uniform along the cavity length (max. $T_{ZnO\text{-}surface}$ = 2126 K) and decrease across the insulating material and close to the water-cooled aperture and quench. The solar-to-chemical energy conversion efficiency η, defined by Eq. (17) and calculated by integration over the day, is 50% and 56% for the 100 and 1000 kW reactors, respectively. The sensible heat term of Eq. (17), i.e. the solar thermal energy consumed to heat the reactants from ambient to the reaction temperature, represents 8.9% and 10.1% of P_{solar} for the 100 and 1000 kW reactors, respectively. η is practically insensitive to the variation of β from 1900 to 7850 m^{-1}, with a slight increase due to the lower $k_{radiative}$. In contrast, η decreases relatively by 15% when p is varied from 0.5 to 0 due to a decrease in $k_{conductive}$ and in the volume of reacting ZnO.

Table 3 lists the energy balances for the 10, 100, and 1000 kW reactors. The major sources of irreversibility are those derived from heat losses by re-radiation through the aperture, which, to some extent, can be reduced by increasing the incident solar radiative flux and, consequently, reducing the aperture size. The incorporation of secondary non-imaging concentrators, e.g. compound parabolic concentrators [27] has the potential of boosting the solar concentration ratio by a factor of $1/\sin^2\alpha$, where α denotes the rim angle of the incoming solar radiation. The sensible heat of the hot products Zn(g) and O_2 exiting the reactor is assumed lost during the quenching for avoiding their recombination [28]. Alternatively, electrothermal methods for in situ separation of Zn(g) and O_2 at high temperatures may allow partial recovery of the sensible heat in separate streams [29]. The significantly higher value of η predicted for the 100 and 1000 kW reactors as compared to that measured for the 10 kW reactor is primarily due to higher $T_{ZnO\text{-}surface}$ (higher by about 200 K) and, consequently, significantly higher reaction rates, and to a reduction of the conduction losses through optimization of the geometry to minimize water-cooled components.

The influence of $T_{ZnO\text{-}surface}$ on the energy conversion efficiency was examined by varying $P_{solar,nominal}$ in the range 50–100 kW for the 100 kW reactor, and in the range 500–1000 kW for the 1000 kW

Table 3
Dimensions and energy balance for the 10 kW prototype reactor, and for the 100 and 1000 kW scaled-up reactors.

	10 kW		100 kW	1000 kW
Aperture diameter, mm	60		190	600
Window diameter, mm	240		370	790
Cavity diameter, mm	160		500	1600
Cavity length, mm	230		750	2400
Cavity outlet diameter, mm	80	30	80	260
Insulation thickness, mm	120		200	200
Mantle thickness, mm	3 (Al)		5 (steel)	10 (steel)
η	1.1%	16.9%	50.0%	55.9%
r_{mean}, kg h^{-1}	0.049	0.745	25.2	282.5
Sensible heat	13.1%	18.6%	20.5%	20.1%
Re-radiation	30.2%	29.7%	17.5%	17.6%
Conduction	46.7%	22.1%	6.6%	2.5%
Convection	8.9%	12.7%	5.4%	3.9%

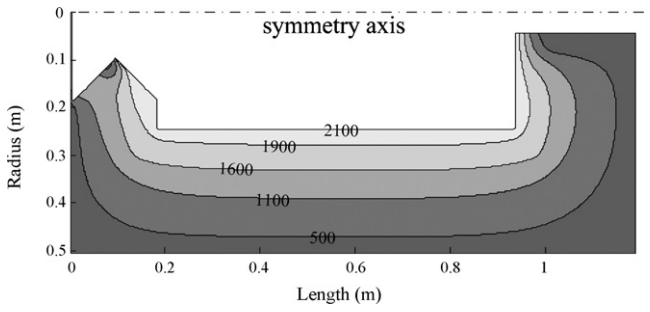

Fig. 5. Temperature contour plot (in K) of the 100 kW reactor at t = 7 h.

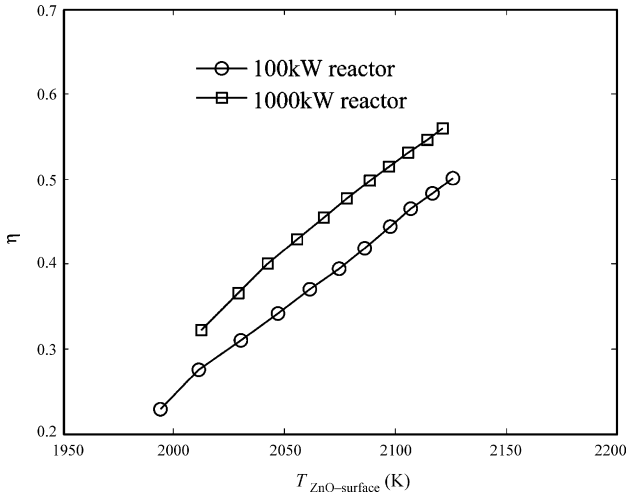

Fig. 6. The solar-to-chemical energy conversion efficiency η as a function of ZnO surface temperature $T_{\text{ZnO-surface}}$ for the 100 and 1000 kW reactors. Variation of $T_{\text{ZnO-surface}}$ is obtained by varying $P_{\text{solar,nominal}}$ in the ranges 50–100 kW and 500–1000 kW.

reactor. η is plotted as a function of $T_{\text{ZnO-surface}}$ in Fig. 6. For the 100 kW reactor, η increases from 23% to 50% as P_{solar} increases from 50 to 100 kW and $T_{\text{ZnO-surface}}$ from 1994 to 2126 K. An increase of $T_{\text{ZnO-surface}}$ by about 100 K to 2094 K results in a remarkable increase of η by 21% to 44%. A similar conclusion is obtained for the 1000 kW reactor as shown in Fig. 6.

6. Summary and conclusion

A transient heat transfer model has been formulated to simulate a solar cavity-receiver lined with a shrinking layer of ZnO particles that are directly exposed to concentrated solar radiation and undergo thermal dissociation. The radiosity and Monte Carlo methods were applied to obtain the distribution of net radiative fluxes, and the finite volume method with the explicit Euler time integration scheme were applied to solve the unsteady energy conservation equation that links conductive, convective, and radiative heat transfer to the rate of the reaction. Experimental validation was accomplished with a 10 kW prototype in terms of temperatures and reaction extents for 4 experimental runs with multiple feed-cycles. The ZnO dissociation reaction occurred in the topmost layers which is typical of an ablation regime, as radiative transfer to the endothermic reaction proceeded at a faster rate than heat conduction across the ZnO layer and insulation. Scaling up the reactor to 100 and 1000 kW nominal solar power input has the potential of reaching maximum solar-to-chemical conversion efficiencies exceeding 50%, mainly as a result of higher reaction rates at higher operating temperatures and a reduction in the conduction losses through optimization of the geometry to minimize water-cooled components.

Acknowledgments

Financial support by the Swiss Federal Office of Energy (SFOE) is gratefully acknowledged. We thank H. Friess and P. Coray for computational support, and A. Frei, D. Gstoehl, A Meier and D. Wuillemin for technical support during the experimental campaign.

References

[1] A. Steinfeld, Solar thermochemical production of hydrogen—a review, Solar Energy 78 (5) (2005) 603–615.
[2] T. Kodama, Y. Nakamuro, T. Mizuno, A two-step thermochemical water splitting by iron-oxide on stabilized zirconia, Journal of Solar Energy Engineering 128 (1) (2006) 3–7.
[3] S. Abanades, G. Flamant, Thermochemical hydrogen production from a two-step solar-driven water-splitting cycle based on cerium oxides, Solar Energy 80 (12) (2006) 1611–1623.
[4] M. Roeb, C. Sattler, R. Klüser, N. Monnerie, L.d. Oliveira, A.G. Konstandopoulos, C. Agrafiotis, V. Zaspalis, L. Nalbandian, A. Steele, P. Stobbe, Solar hydrogen production by a two-step cycle based on mixed iron oxides, Journal of Solar Energy Engineering 128 (2) (2006) 125–133.
[5] S. Abanades, P. Charvin, F. Lemont, G. Flamant, Novel two-step SnO_2/SnO water-splitting cycle for solar thermochemical production of hydrogen, International Journal of Hydrogen Energy 33 (21) (2008) 6021–6030.
[6] C. Perkins, A.W. Weimer, Likely near-term solar-thermal water splitting technologies, International Journal of Hydrogen Energy 29 (15) (2004) 1587–1599.
[7] A. Steinfeld, Solar hydrogen production via a two-step water-splitting thermochemical cycle based on Zn/ZnO redox reactions, International Journal of Hydrogen Energy 27 (6) (2002) 611–619.
[8] F.O. Ernst, A. Tricoli, S.E. Pratsinis, A. Steinfeld, Co-synthesis of H_2 and ZnO by in situ Zn aerosol formation and hydrolysis, AIChE Journal 52 (9) (2006) 3297–3303.
[9] R. Palumbo, M. Keunecke, S. Möller, A. Steinfeld, Reflections on the design of solar thermal chemical reactors: thoughts and transformation, Energy 29 (5) (2004) 727–744.
[10] S. Abanades, P. Charvin, G. Flamant, Design and simulation of a solar chemical reactor for the thermal reduction of metal oxides: case study of zinc oxide dissociation, Chemical Engineering Science 62 (22) (2007) 6323–6333.
[11] L.O. Schunk, P. Haeberling, S. Wepf, D. Wuillemin, A. Meier, A. Steinfeld, A receiver-reactor for the solar thermal dissociation of zinc oxide, Journal of Solar Energy Engineering 130 (2) (2008) 021009.
[12] R. Müller, W. Lipiński, A. Steinfeld, Transient heat transfer in a directly-irradiated solar chemical reactor for the thermal dissociation of ZnO, Applied Thermal Engineering 28 (5–6) (2008) 524–531.
[13] L.O. Schunk, W. Lipiński, A. Steinfeld, Ablative heat transfer in a shrinking packed-bed of ZnO undergoing thermal dissociation, AIChE Journal.
[14] L.O. Schunk, A. Steinfeld, Kinetics of the thermal dissociation of ZnO exposed to concentrated solar irradiation using a solar-driven thermogravimeter in the 1800–2100 K range, AIChE Journal, in press.
[15] J. Petrasch, P. Coray, A. Meier, M. Brack, P. Haberling, D. Wuillemin, A. Steinfeld, A novel 50 kW 11,000 suns high-flux solar simulator based on an array of xenon arc lamps, Journal of Solar Energy Engineering 129 (4) (2007) 405–411.
[16] A. Roine, Outokumpu HCS Chemistry 5.11, Outokumpu Research Oy, 2002.
[17] R. Siegel, J. Howell, Thermal Radiation Heat Transfer, Taylor & Francis, New York, London, 2002.
[18] P. Zehner, E.U. Schlünder, Wärmeleitfähigkeit von Schüttungen bei mäßigen Temperaturen, Chemie Ingenieur Technik - CIT 42 (14) (1970) 933–941.
[19] ANSYS CFX 10.0, http://www.cfx-germany.com.
[20] B. Özerdem, Measurement of convective heat transfer coefficient for a horizontal cylinder rotating in quiescent air, International Comunications in Heat and Mass Transfer 27 (3) (2000) 389–395.
[21] F.P. Incropera, D.P. DeWitt, Fundamentals of Heat and Mass Transfer, John Wiley & Sons, New York, 1996.
[22] Y.R. Shieh, C.J. Li, Y.H. Hung, Heat transfer from a horizontal wafer-based disk of multi-chip modules, International Journal of Heat and Mass Transfer 42 (6) (1999) 1007–1022.
[23] J. Petrasch, Thermal modeling of solar chemical reactors: transient behavior, radiative transfer, MS Thesis, ETH Zürich, 2002.
[24] R. Müller, A. Steinfeld, Band-approximated radiative heat transfer analysis of a solar chemical reactor for the thermal dissociation of zinc oxide, Solar Energy 81 (10) (2007) 1285–1294.
[25] T. Osinga, W. Lipiński, E. Guillot, G. Olalde, A. Steinfeld, Experimental determination of the extinction coefficient for a packed-bed particulate medium, Experimental Heat Transfer 19 (1) (2006) 69–79.
[26] L.A. Dombrovsky, H.K. Tagne, D. Baillis, L. Gremillard, Near-infrared radiative properties of porous zirconia ceramics, Infrared Physics & Technology 51 (1) (2007) 44–53.
[27] W.T. Welford, R. Winston, High Collection Nonimaging Optics, Academic Press, San Diego, 1989.
[28] D. Gstoehl, A. Brambilla, L.O. Schunk, A. Steinfeld, A quenching apparatus for the gaseous products of the solar thermal dissociation of ZnO, Journal of Materials Science 43 (14) (2008) 4729–4736.
[29] E.A. Fletcher, Solarthermal and solar quasi-electrolytic processing and separations: zinc from zinc oxide as an example, Industrial & Engineering Chemistry Research 38 (6) (1999) 2275–2282.
[30] MPDB 5.50, JAHM Software, 1999.
[31] Rath Group, www.rath-group.com, product #: Kerform KVS 1800/400.
[32] T. Olorunyolemi, A. Birnboim, Y. Carmel, O.C. Wilson, I.K. Lloyd, Thermal conductivity of zinc oxide: from green to sintered state, Journal of American Ceramic Society 85 (5) (2002) 1249–1253.